Chinese Chemical Letters 34 (2023) 107885

Contents lists available at ScienceDirect

Chinese Chemical Letters

journal homepage: www.elsevier.com/locate/cclet

Accelerated discovery of novel high-performance zinc-ion battery cathode materials by combining high-throughput screening and experiments

Haoran Luo[a,1], Jiangbin Deng[a,1], Qianzhi Gou[a], Omololu Odunmbaku[a], Kuan Sun[a], Juanxiu Xiao[b], Meng Li[a,*], Yujie Zheng[a,*]

[a] MOE Key Laboratory of Low-grade Energy Utilization Technologies and Systems, School of Energy and Power Engineering, Chongqing University, Chongqing 400044, China

[b] State Key Laboratory of Marine Resource Utilization in South China Sea, School of Chemical Engineering and Technology, Hainan University, Haikou 570228, China

ARTICLE INFO

Article history:
Received 29 August 2022
Revised 23 September 2022
Accepted 4 October 2022
Available online 10 October 2022

Keywords:
Aqueous zinc ion battery
Spinel
High-throughput
First-principles calculations
Experiment
Accelerate

ABSTRACT

Aqueous zinc ion batteries (AZIBs) have attracted much attention in recent years due to their high safety, low cost, and decent electrochemical performance. However, the traditional electrodes development process requires tedious synthesis and testing procedures, which reduces the efficiency of developing high-performance battery devices. Here, we proposed a high-throughput screening strategy based on first-principles calculations to aid the experimental development of high-performance spinel cathode materials for AZIBs. We obtained 14 spinel materials from 12,047 Mn/Zn-O based materials by examining their structures and whether they satisfy the basic properties of electrodes. Then their band structures and density of states, open circuit voltage and volume expansion rate, ionic diffusion coefficient and energy barrier were further evaluated by first-principles calculations, resulting in five potential candidates. One of the promising candidates identified, Mg_2MnO_4, was experimentally synthesized, characterized and integrated into an AZIB based cell to verify its performance as a cathode. The Mg_2MnO_4 cathode exhibits excellent cycling stability, which is consistent with the theoretically predicted low volume expansion. Moreover, at high current density, the Mg_2MnO_4 cathode still exhibits high reversible capacity and excellent rate performance, indicating that it is an excellent cathode material for AZIBs. Our work provides a new approach to accelerate the development of high-performance cathodes for AZIBs and other ion batteries.

Lithium-ion batteries (LIBS) have dominated the power source electronic devices and electric vehicles (EVs) in the modern society. However, the possible safety issues deriving from organic electrolyte and shortage of lithium source inevitably prompt researchers to search for the substitutes for LIBs [1–3]. Recently, aqueous zinc ion batteries (AZIBs) have attracted various research interest due to their high safety, low standard electrode potential (−0.76 V *vs.* SHE), and high volumetric capacity (5851 mAh/cm^3) [4–9]. As the key component for AZIBs, cathode has a prominent influence on the capacity, cycling stability and rate performance for the entire battery. However, the cathodes currently suffer from faces problems of electrode dissolution, low intrinsic conductivity, and sluggish slow mass transfer reaction, thus degrading which limit the further improvement of the application prospect performance of AZIBs [10–14]. Therefore, it's desirable to develop the suitable cathode for AZIBs.

Among various candidates, spinel materials are considered as one of the suitable candidates for AZIBs due to the low price, tunable structure, favorable structural stability, and high open circuit voltage [15–18]. Normally, the chemical formula of spinel materials is denoted as AB_2X_4, where the A and B ions are tetrahedral coordination and octahedron coordination, respectively, and X can be an anion of O, S, Se or Te [19]. According to the distribution of cations, spinel can be divided into three types: normal, inverse, and complex spinels [20,21]. Benefiting from the unique structure and superior physicochemical property, spinel-based cathode materials have been diffusely applied in the field of AZIBs. For example, Yuan *et al.* reported a novel Mg_2MnO_4 active material

* Corresponding authors.
E-mail addresses: limeng@cqu.edu.cn (M. Li), zhengyujie@cqu.edu.cn (Y. Zheng).
[1] These authors contributed equally to this work.

https://doi.org/10.1016/j.cclet.2022.107885
1001-8417/

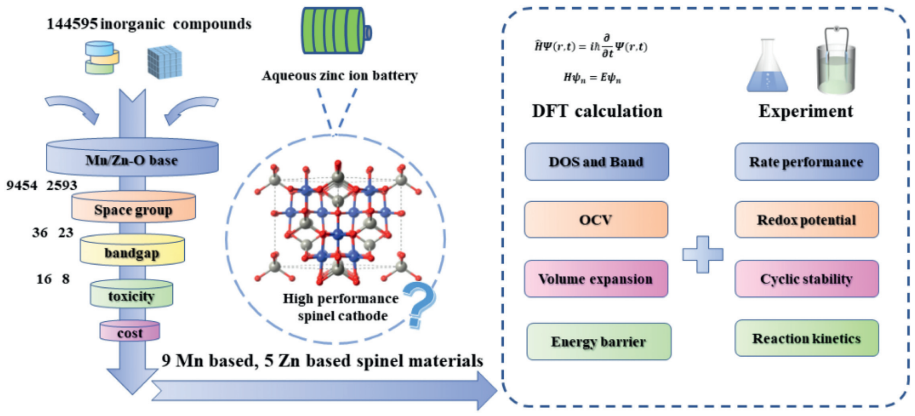

Fig. 1. Schematic diagram of the development of high-performance spinel cathode materials by combining DFT-based high-throughput screening and experiments.

with inverse-spinel structure and utilized it as cathode for AZIBs [22]. Owing to the presence of rich high-valence-state Mn^{4+}, the as-constructed Zn//Mg_2MnO_4 battery exhibits superior Zn^{2+} storage ability. In addition, Zhang *et al.* reported a non-stoichiometric $ZnMn_2O_4$@C cathode which exhibits high specific capacity (~150 mAh/g at 50 mA/g), long-term cyclability and superior rate capability [23].

Despite these advancements, the most development of spinel-based cathode in AZIBs is based on traditional experimental methods. This process inevitably increases the time and cost of developing new electrode, thereby leading to the insufficient efficiency [24–26]. Therefore, it is necessary to search for a more efficient and convenient method to identify suitable candidates for AZIB cathodes from a large number of spinel materials. Recently, the continuous development of computers techniques and theoretical models have provided a high-efficiency avenue for exploring the energy storage mechanism of new electrode materials. Specially, a variety of high-throughput screening methods for new materials have been extensively reported, which can greatly shorten the period and cost of developing new materials [27–30]. As a typical example, Scott *et al.* combined the high-throughput density functional theory (DFT) calculations and automatic grand canonical linear programming (GCLP) method to acquire 16 high-performance anode materials for lithium-ion batteries by predicting several key performance indicators: open circuit voltage, volume change per lithium addition, gravimetric and volumetric capacities [31]. Similarly, Cai *et al.* utilized the high-throughput combined with machine learning method to screen spinel containing Mg/Zn elements as cathode materials for organic-based magnesium/zinc ion batteries, and reported six new spinel materials with high conductivity, high ion diffusion rate and low volume expansion rate [32]. However, there are few works reported the application of high-throughput screening method to design the cathode for AZIBs.

In this paper, we proposed a DFT-based high-throughput screening method combined with experimental validation to enable rapid development of high-performance spinel cathode material for AZIBs. Firstly, 9 Mn-based and 5 Zn-based spinel materials form 12,047 Mn/Zn-O based materials were obtained by checking their structures and whether they satisfy the basic properties of electrodes. Then, five candidates were obtained by further evaluating their electronic structure, open circuit voltage, volume expansion rate, and ionic diffusion coefficient, *etc.* by first-principles calculations. Meanwhile, taking Mg_2MnO_4 (one of the five candidates) as an example, we verified the performance of Mg_2MnO_4-based AZIBs. The cycling stability, reversible capacity, and rate performance of Mg_2MnO_4-based AZIBs are all excellent. Both electrochemical kinetics characterization and computational results show that the Mg_2MnO_4 cathode possesses excellent rate capability due to its fast reaction kinetics and low activation energy for ion migration. Therefore, all our results suggest that high-throughput screening based on first-principles calculations can assist us to experimentally obtain promising AZIBs cathode materials and greatly improve the development efficiency.

Fig. 1 shows the basic procedure of high-throughput computing method combined with experiments. Firstly, using the Python-based *matminer* Discovery Framework tool [33], we extracted all oxides containing Zn/Mn elements from the Materials Projects [34–36] database containing a total of 144,595 inorganic compounds. A total of 9454 Mn-O-based compounds and 2593 Zn-O-based compounds were obtained. The space group determines the internal arrangement of the crystal lattice, and our targets are spinel materials whose space group is Fd-3m. Through the discriminant screening of their space groups, 36 Mn-based and 23 Zn-based spinel oxides were obtained. Then, we obtained a total of 16 Mn-based and 8 Zn-based spinel materials by determining whether their band gaps are zero. Finally, comprehensively considering toxicity, commonness and price of the elements (Eu, Sc, Hy, Dy, Ag, Pd), 9 Mn-based and 5 Zn-based spinel materials were finally determined for further verification. In respond to the 14 selected spinel materials, we further calculated their microscopic properties directly related to their electrochemical performance when used as electrodes, including density of states, band structure, open circuit voltage, volume expansive ratio, ion diffusion coefficient, and energy barrier. To verify the computational results, we also selected a representative material for experimental synthesis and battery device application.

The calculated density of states and bands structures of the 14 spinel materials are shown in Fig. 2 ($LiMn_2O_4$, Mg_2MnO_4, $ZnCu_2O_4$ and $ZnNi_2O_4$) and Fig. S1 (Supporting information, Mn_2AlO_4, Mn_2CuO_4, Mn_2NiO_4, $MnCo_2O_4$, MnV_2O_4, $NaMn_2O_4$, Ti_2MnO_4, Mn_2ZnO_4, Ti_2ZnO_4, V_2ZnO_4) [37]. It can be seen that the valance and conduction bands of these 14 spinel materials are continuous around the Fermi level, confirming that they have the excellent electrical conductivity, which is consistent with the expectation of high-throughput screening.

As mentioned previously, to validate the high-throughput screening strategy based on first-principles predictions, we need to select a representative material for experimental testing. Considering the simple fabrication process and admirable electrochemical performance [22,38], and also as one of the promising candidates based on our theoretical predictions (Fig. S2 in Supporting information, we comprehensively compared the as-obtained 8 spinel materials from the aspect of OCV, volume expansion, energy barrier, as well as synthesis), Mg_2MnO_4 was selected as representative to explore its Zn^{2+} storage ability. We synthesized the Mg_2MnO_4 material and constructed the coin cell to measure its

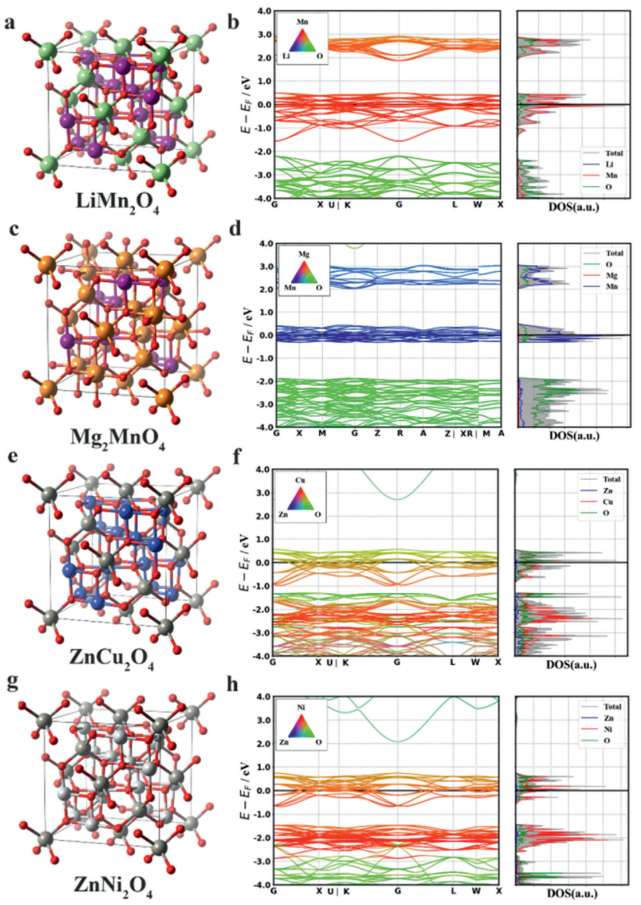

Fig. 2. Atomic structure, band structure and DOS of the 4 selected spinel materials, including (a, b) $LiMn_2O_4$, (c, d) Mg_2MnO_4, (e, f) $ZnCu_2O_4$ and (g, h) $ZnNi_2O_4$. Green: Li, purple: Mn, yellow: Mg, blue: Cu, gray: Zn, white: Ni, red: O.

electrochemical performance, and the preparation process is exhibited in Fig. 3a. Firstly, the X-ray diffraction (XRD) pattern was conducted to characterize the sample's crystal structure. As depicted in Fig. 3b, all the characteristic diffraction peaks can match well with the standard Mg_2MnO_4 phase (JCPDS No. 19–0773), indicating the successful synthesis of electrode materials. In addition, the element composition and valence states of the Mg_2MnO_4 sample are analyzed by X-ray photoelectron spectroscopy (XPS). As illustrated in Fig. S3 (Supporting information), XPS spectra affirmed the existence of Mn, Mg, and O elements in the Mg_2MnO_4 composite. For Mn 2p spectrum (Fig. 3c), two distinct peaks centered at 641.5 eV and 653.2 eV can be assigned to Mn $2p_{3/2}$ and Mn $2p_{1/2}$, respectively. The spin energy difference of 11.7 eV, indicating that the manganese element mainly exists in the form of Mn^{4+} in the sample [39–41]. In addition, the high-resolution Mg 1s spectra also displays a distinct peak situated in 1302.6 eV (Fig. 3d) which originates from the Mg^{2+}. All the afore-said results are consistent with the XRD analysis, further suggesting the successful formation of Mg_2MnO_4 phase.

The morphology and microstructure of the as-fabricated samples were characterized by scanning electron microscopy (SEM) and transmission electron microscopy (TEM) [42]. The SEM-EDS pattern in Fig. 3e shows that the elements Mg, Mn and O are uniformly distributed in Mg_2MnO_4. According to EDS mapping (Fig. S4 and Table S1 in Supporting information), the ratio of Mn to Mg is calculated to be 0.433:1, which is close to the 1:2. In addition, the element content in the Mg_2MnO_4 sample was also estimated using the inductively coupled plasma-optical emission spectrometer (ICP-OES) technique. As summarized in Table S2 (Supporting information), the molar ratio of Mg and Mn is 0.08 to 0.043, which is consistent with the EDS mapping, further confirming the existence of Mg_2MnO_4 phase. Subsequently, the micro-structure of the Mg_2MnO_4 material was characterized by TEM and shown in Fig. 3f and Fig. S5 (Supporting information). Obviously, the as-prepared Mg_2MnO_4 sample exhibit uniform nanosheets connected to form nanorods. Lattice stripes were observed by high-resolution transmission electron microscopy (HRTEM) and the spacing of the lattice stripes is about 0.22 nm (Fig. 3g), which corresponding to the characteristic crystal plane (400) of Mg_2MnO_4. All the characterization results confirmed the successful synthesis of Mg_2MnO_4.

To further explore the performance of these spinel materials as cathodes, as shown in Fig. S6 (Supporting information), we calculated the open circuit voltage (OCV) generated when 2, 4 and 6 Zn^{2+}were intercalated. The definition of OCV is as follows [43]:

$$V_{OC} = -\frac{E_{cathod}(x_2) - E_{cathod}(x_1) - (x_2 - x_1)E_{Zn}}{(x_2 - x_1)N} \quad (x_2 > x_1) \qquad (1)$$

where x_1 and x_2 represent the number of embedded Zn^{2+}, E_{cathod} represents the energy of the electrode when embedded with different number of Zn^{2+}, E_{Zn} represents the energy of a single zinc atom, and N represents the valence of the embedded ions. Firstly, we checked the stability of the embedded sites. Taking Mg_2MnO_4 as an example, we found that the two embedded Zn^{2+} were more stable when they were located on opposite surfaces. The sites and their corresponding energies of the Zn^{2+} embedded in the Mg_2MnO_4 are summarized in Fig. S7 and Table S2 (Supporting information). Only 8 spinel materials were found to exhibit voltage by OCV calculations and their average voltages are summarized in Fig. 4a. We can see 7 of them have average voltages above 0.5 V, which can be considered as high-voltage electrode materials [44]. Among them, as exhibited in Fig. 4b, $ZnCu_2O_4$ and $ZnNi_2O_4$ exhibit the best performance with the average OCV reaching 1.775 and 0.963 V, respectively. The voltages of other materials with different numbers of Zn^{2+} embedded are summarized in Fig. S8 (Supporting information). Need to note that, the average voltage of Mg_2MnO_4 is 0.6 V, indicating that it is also a high voltage material, which is further confirmed by the cyclic voltammetry (CV) profiles of Mg_2MnO_4 electrode in Mg_2MnO_4//Zn coin cells (Fig. 4c). During the first cathodic scan, two obvious reduction peaks situated at 1.34 and 1.18 V can be detected which are ascribed to the insertion of H^+ and Zn^{2+}, respectively, whereas the oxidation peak around 1.6 V is corresponding to the ionic extraction behavior. In the subsequent cycles, all the CV curves well overlap, demonstrating the superior reversibility. Furthermore, the galvanostatic charge/discharge (GCD) curves shown in Fig. 4d are consistent with the CV curves, which show an average discharge voltage of about 1.35 V and a discharge capacity of 358.8 mAh/g at 200 mA/g after 50 cycles. The charge-discharge curves at other current densities can be found in Fig. S9 (Supporting information). Obviously, the relevant charge and discharge platform and the redox peaks in the CV curve can be well matched. For example, the discharge platform at 1.5 and 1.3 V is ascribed to the ion insertion behavior, whereas the charge platform of 1.6 V corresponds to the ionic extraction behavior.

Moreover, we also calculated the volume expansion changes of the spinel materials after embedding Zn^{2+}, which is related to the cycling stability of AZIBs. In normal, the low volume expansion rate indicates the admirable cycling stability. As summarized in Fig. 4e, the volume expansion rate of all 8 materials is less than 20%, indicating that all of them possess outstanding structural stability from the viewpoint of theory [32]. In particular, the Mg_2MnO_4 and $NaMn_2O_4$ model exhibit very low volume expansions (*e.g.*, less than 5%). The experimental cycling stability measurements are shown in Fig. 4f and Fig. S10 (Supporting information), Mg_2MnO_4

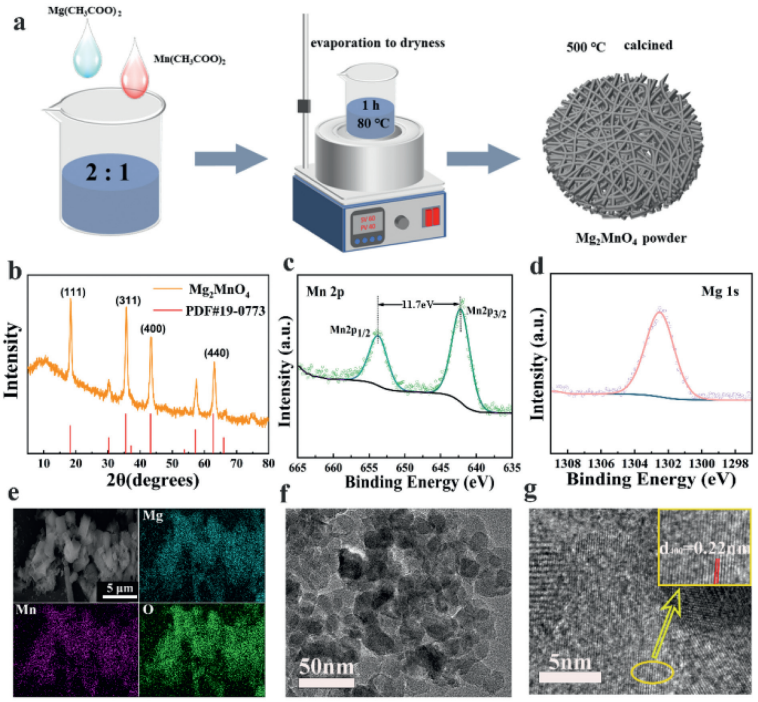

Fig. 3. (a) Preparation process of spinel Mg_2MnO_4. (b) XRD patterns of Mg_2MnO_4. XPS of (c) Mn 2p and (d) Mg 1s for Mg_2MnO_4 material, respectively. (e) SEM-EDS mapping images and (f) TEM image of Mg_2MnO_4. (g) Lattice spacing in Mg_2MnO_4 crystal.

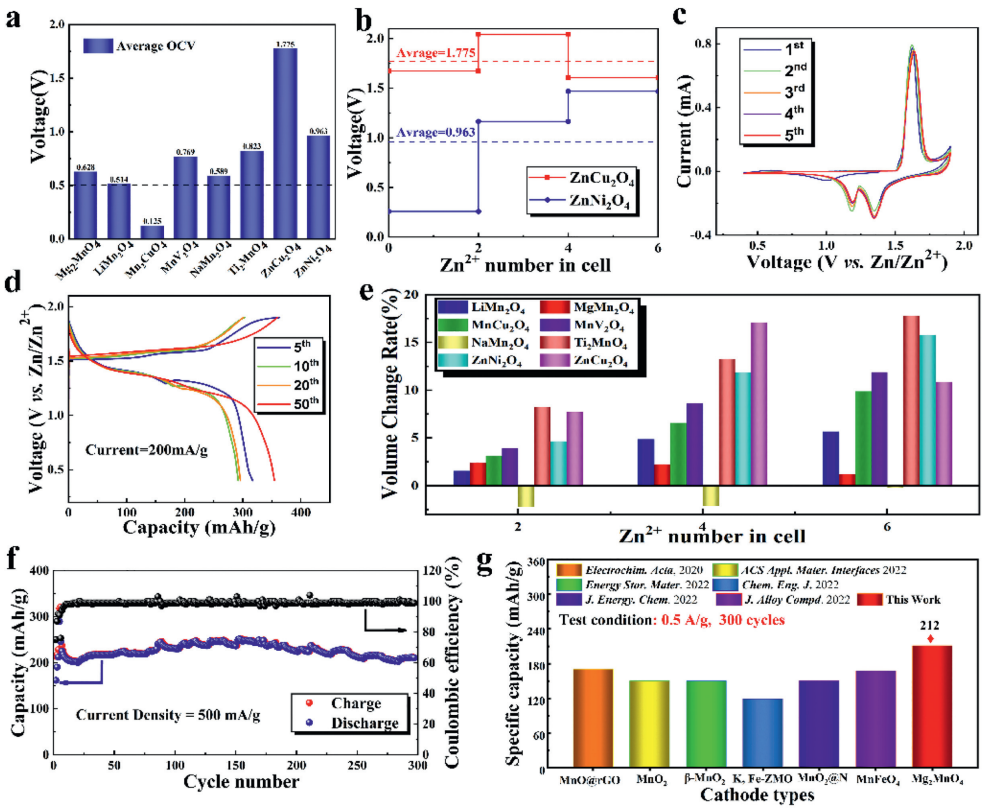

Fig. 4. (a) Average open circuit voltage of 8 materials. (b) Voltage of $ZnCu_2O_4$ and $ZnNi_2O_4$ when different ions are embedded. (c) The CV curves of Zn//Mg_2MnO_4 battery at 0.2 mV/s. (d) The galvanostatic charge-discharge curves at 200 mA/g. (e) The volume expansion ratio of the 8 spinel materials. (f) Cycling stability at 500 mA/g for Zn//Mg_2MnO_4 battery. (g) Cycling performance comparison between Mg_2MnO_4 and other cathode materials.

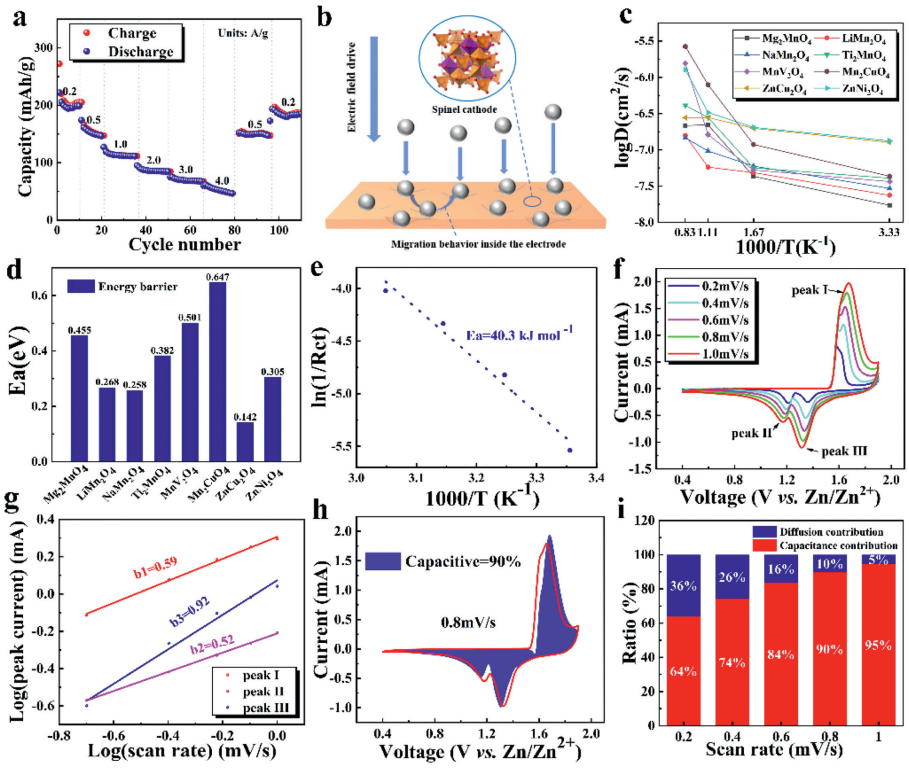

Fig. 5. (a) Rate performance of the Mg_2MnO_4 cathode. (b) Schematic diagram of diffusion behavior of Zn^{2+} at the electrode. (c) The ion diffusion of 8 spinel materials at 300, 600, 900 and 1200 K. (d) Energy barrier of the Zn^{2+} in 8 spinel materials. (e) Fitted activation energy. (f) CV curves of Zn//Mg_2MnO_4 battery with different scan rates. (g) log(peak current) *vs.* log(scan rate) plots of three peaks in CV curves. (h) The corresponding capacitive contribution of Mg_2MnO_4 at 0.8 mV/s. (i) Capacitance contribution ratio at different scan rates.

electrode exhibits high cycling stability at 500 mA/g for 300 cycles and 200 mA/g for 100 cycles. Finally, as shown in Fig. 4g, we can see that the Mg_2MnO_4 cathode does exhibit superior capacity retention and excellent cycling stability (212 mAh/g at 0.5 A/g, 300 cycles) after comparing the cycling performance of Mg_2MnO_4 with other cathode materials [45–50].

In addition, the rate performance of Mg_2MnO_4//Zn full cell is also conducted, as illustrated in Fig. 5a. According to the results of the rate performance, we calculated the energy density (cathode only) at power densities of 428.5 W/kg and 2857.1 W/kg, which were 578.1 Wh/kg and 224.1 Wh/kg, respectively. As summarized in Fig. S11 (Supporting information), by comparing the related values of energy and power density, it is found that our Mg_2MnO_4 cathode has better performance than the previously manganese-based cathodes. With the increasement of current densities, the reversible specific capacity of Mg_2MnO_4 shows favorable stability. When the current density attains to 4 A/g, the battery system could have a high capacity of 70 mAh/g. When the current density is back to 0.2 A/g, the capacity retention ratio exceeds 100%. These results indicated that it has high conductivity and fast ion diffusion efficiency. In order to check its electrochemical kinetics, we further investigate the diffusion behavior of Zn^{2+} (Fig. 5b), the diffusion of Zn^{2+} at the electrode driven by the electric field can be divided into the diffusion between the electrolyte-electrode interface and the diffusion inside the electrode material. Generally, diffusion inside the electrode dominates due to its larger resistance [51,52]. Therefore, we only focus on the migration of Zn^{2+} inside the spinel materials.

Through *ab initio* molecular dynamics (AIMD) simulations, we investigated the diffusion behavior of Zn^{2+} in these 8 spinel materials. The relationship between logD and 1000/T are summarized in Fig. 5c. The calculated diffusion coefficients of Zn^{2+} in these 8 materials are all greater than 10^{-9} cm^2/s (Table S3 in Supporting information), which indicates that Zn^{2+} can diffuse rapidly in these electrodes. We can calculate the diffusion barriers of Zn^{2+} in these eight spinel materials by fitting the Arrhenius formula [53]. As shown in Fig. 5d, their migration energy barriers are all less than 1 eV, which also indicates that Zn^{2+} can diffuse easily in these electrodes. Moreover, electrochemical impedance spectroscopy (EIS) analysis was performed for Mg_2MnO_4-based battery. As depicted in Fig. S12 (Supporting information), the Nyquist plot consists of a semicircle in the high-frequency region and a sloping line in the low-frequency region, corresponding to the charge transfer resistance (R_{ct}) and the ion diffusion resistance (Z_w), respectively [54]. From the R_{ct} values at different temperatures (Table S4 in Supporting information), the activation energy of the whole reaction process can also be obtained according to the Arrhenius formula [55,56]:

$$\frac{1}{R_{ct}} = A_0 e^{\frac{-E_a}{RT}} \quad (2)$$

where A_0 is a constant factor, T stands for the temperature (K), R is the gas constant (8.314 J mol^{-1} K^{-1}), and E_a represents the activation energy, respectively. As shown in Fig. 5e, the E_a value of 40.3 kJ/mol was obtained by linear fitting of the R_{ct} values at different temperatures, which is also in good agreement with the theoretical result (0.455 eV in Fig. 5d, and 1 eV = 96 kJ/mol).

To understand the charge storage process, the electrochemical kinetics was investigated by testing the CV curves at different scan rates in Fig. 5f. Their peak currents i and scan rate υ satisfy the following equation [57,58]:

$$i = a\upsilon^b \quad (3)$$

where a and b are adjustable parameters. When the value of b is close to 0.5, the reaction process depends on the control of the ion

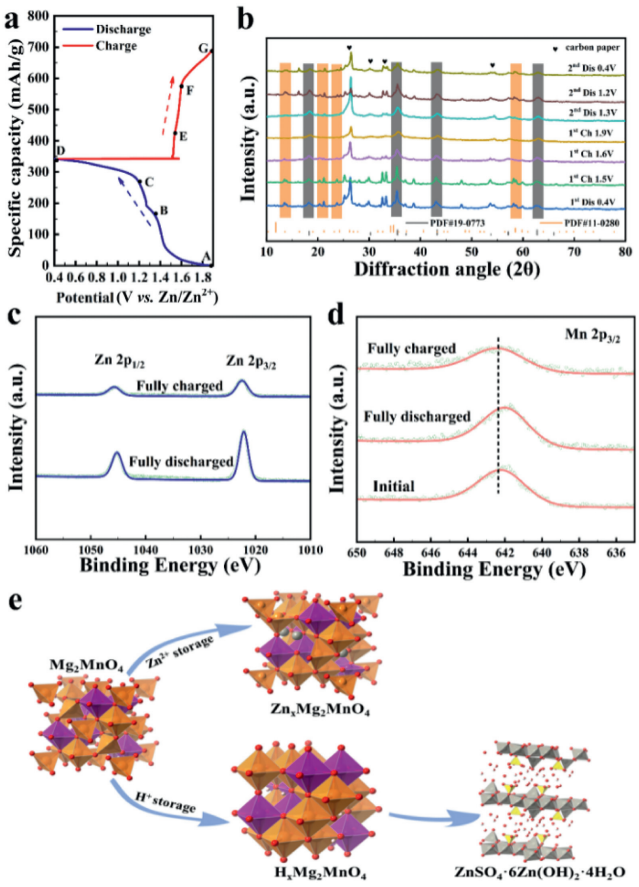

Fig. 6. (a) The second discharge/charge curve of Mg_2MnO_4 cathode at 0.2 A/g, and the marked states were selected for *ex situ* tests. (b)The *ex-situ* XRD patterns of Mg_2MnO_4 in different discharge/charge states. (c, d) The *ex-situ* XPS spectra of Zn 2p and Mn $2p_{3/2}$. (e) Schematic diagram of H^+ and Zn^{2+} insertion mechanism on Mg_2MnO_4 cathode.

diffusion process, while the value of *b* reaches 1, the corresponding electrochemical behavior is controlled by the capacitance. According to the slopes of the log(*i*) *vs.* log(υ) curves for all peaks in Fig. 5g, the *b* values for peaks I, II and III are 0.59, 0.52 and 0.92, respectively, which implies that the combination of ion diffusion and capacitive behavior synergistically controls the charge storage process. Synergistic effects of diffusion and capacitance are favorable for fast ion diffusion kinetics. In addition, the capacitance contribution can be calculated according to the following equation [42,59,60]:

$$i = k_1\upsilon + k_2\upsilon^{1/2} \quad (4)$$

where *i* is the current (mA), υ corresponds to the scan rate (mV/s), $k_1\upsilon$ corresponds to the current contributed by the capacitor and $k_2\upsilon^{1/2}$ corresponds to the current contributed by diffusion. According to Eq. 4, the capacitance contribution at different sweep speeds can be obtained. The shaded part of Fig. 5h represents the capacitance contribution at 0.8 mV/s. The capacitance contributions at all scan rate are displayed in Fig. 5i. The high capacitance contributions with increasing scan rate indicate fast ion transfer kinetics, corresponding to the good rate performance of the Mg_2MnO_4 material.

According to the above analysis, the Mg_2MnO_4 cathode showed excellent electrochemical ability. To further understand the relevant ion storage mechanism, *ex situ* XRD and XPS were performed on the Mg_2MnO_4 cathode. The GCD curves of the Mg_2MnO_4 cathode in different states in the second cycle are shown in Fig. 6a. Combined with the *ex situ* XRD results (Fig. 6b), it can be seen that the diffraction peak of $ZnSO_4{\cdot}6Zn(OH)_2{\cdot}4H_2O$ (JCPDS No. 11–0280) disappears after charging from 0.4 V to 1.6 V, and appears after discharging from 1.9 V to 1.3 V. These results confirm that H^+ and Zn^{2+} are reversibly de-intercalate/intercalate into the Mg_2MnO_4 electrode [60,61]. It is worth noting that the diffraction peaks at about 18.3°, 35.5°, 43.3°, 62.8°, corresponding to the (111), (311), (400) and (440) crystal planes of Mg_2MnO_4 respective, did not show significant changes during the discharging/charging process. This means that the Mg_2MnO_4 cathode has excellent cycle stability. In addition, *ex situ* XPS of Zn 2p further showed that the insertion of Zn^{2+} ingress into/egress from the Mg_2MnO_4 electrode during the discharging/charging process [62]. As shown in Fig. 6c, the peaks at 1045.2 eV and 1022.2 eV correspond to signals of Zn $2p_{1/2}$ and Zn $2p_{3/2}$, respectively. When discharged to 0.4 V, a strong Zn 2p signal was detected, which weakened in the charged state. As depicted in Fig. 6d, compared with the initial state, the peak corresponding to Mn $2p_{3/2}$ in the discharged state shifts to a lower binding energy, indicating that the valence of Mn decreases with the insertion of H^+ and Zn^{2+} into Mg_2MnO_4 [63]. The increase of the binding energy of Mn $2p_{3/2}$ at the charged state indicates the full de-intercalation of H^+ and Zn^{2+}. Therefore, the ion intercalation process of the Mg_2MnO_4 cathode is shown in Fig. 6e, where both H^+ and Zn^{2+} are de-intercalate/intercalate into the Mg_2MnO_4 electrode. The analysis of *ex situ* XPS spectra also confirmed the ion storage mechanism of the Mg_2MnO_4 electrode.

Generally, the electrostatic interaction between ions in the process of Zn^{2+} insertion and extraction will affect the battery performance. Here, we calculate the Electron Localization Function (ELF) to compare the electrostatic interaction of the cathode material with/without Zn^{2+} ions. Fig. S13 (Supporting information) shows the electrostatic potential diagrams at 0.6 d on the (001) plane when 0, 2, 4 and 6 Zn ions are inserted. As shown in the figure, when more Zn^{2+} are in inserted, the variation of electrostatic potential is not obvious, which indicates that the Mg_2MnO_4 framework has a strong electrostatic screening effect [43,64]. The strong dielectric screening effect of Mg_2MnO_4 makes the electrostatic interaction between Zn ions very small during Zn storage, which is another reason why Mg_2MnO_4 shows well performance.

In conclusion, we proposed and demonstrated a high-throughput screening strategy based on first-principles calculations that facilitates the rapid development of high-performance spinel cathode materials for AZIBs. Through high-throughput screening and first-principles calculations, we found that 7 materials (Mg_2MnO_4, $LiMn_2O_4$, $NaMn_2O_4$, $ZnCu_2O_4$, $ZnNi_2O_4$, MnV_2O_4, Ti_2MnO_4) exhibited high average open circuit voltage, and 8 materials (Mg_2MnO_4, $LiMn_2O_4$, $NaMn_2O_4$, $ZnCu_2O_4$, $ZnNi_2O_4$, MnV_2O_4, Ti_2MnO_4, $MnCu_2O_4$) possess high ionic mobility and low volume expansion rate. After taking all the properties into consideration, there are five spinel materials (Mg_2MnO_4, $LiMn_2O_4$, $NaMn_2O_4$, $ZnCu_2O_4$, $ZnNi_2O_4$) that have the potential to be used as cathode materials for high-performance AZIBs. Meanwhile, we experimentally synthesized Mg_2MnO_4 and applied it to AZIBs cathode. The Mg_2MnO_4-based battery still has a stable capacity retention of 99% after 300 cycles at a current density of 0.5 A/g, showing good cycling stability, which is consistent with our calculated low volume expansion rate. Both computational and experimental electrochemical kinetics results show that Mg_2MnO_4 material has high capacitive contribution and a low ion migration activation energy, indicating that the material has fast ion transfer kinetics and thus exhibits good rate performance. The agreement between theoretical calculations and experimental results confirms the effectiveness of our high-throughput material screening strategy, which will significantly reduce the development time and cost of AZIBs cathode materials and make obtaining perfect cathode materials more achievable. We believe that this high-throughput screening strat-

egy based on first-principles calculations should also be applicable to the development of other ionic cathode materials.

Declaration of competing interest

The authors declare that they have no known competing financial interests or personal relationships that could have appeared to influence the work reported in this paper.

Acknowledgments

This work was financially supported by research grants from the Natural Science Foundation of China (Nos. 12004057, 62074022, 52173235), Support plan for Overseas Students to Return to China for Entrepreneurship and Innovation (No. cx2020075), Open Fund of Key Laboratory of Low-grade Energy Utilization Technologies and Systems (No. LLEUTS-2020008), Chongqing Funds for Distinguished Young Scientists (No. cstc2021jcyj-jqX0015), Chongqing Talent Plan (No. CQYC2021059206), Fundamental Research Funds for the Central Universities (No. 2020CDJQY-A055).

Supplementary materials

Supplementary material associated with this article can be found, in the online version, at doi:10.1016/j.cclet.2022.107885.

References

[1] Q. Gou, J. Xu, H. Luo, et al., Electrochim. Acta 431 (2022) 141127.
[2] Q. Gou, C. Li, X. Zhang, et al., Energy Technol. 7 (2019) 1800761.
[3] P. Liu, W. Liu, K. Liu, Carbon Energy 4 (2022) 60–76.
[4] Q. Gou, H. Luo, Y. Zheng, et al., Small 18 (2022) 2201732.
[5] J. Zhou, A. Dong, L. Du, et al., Chem. Eng. J. 421 (2021) 127770.
[6] M. Du, C. Liu, F. Zhang, et al., Adv. Sci. 7 (2020) 2000083.
[7] Y. Lu, J. Wang, S. Zeng, et al., J. Mater. Chem. A 7 (2019) 21678–21683.
[8] C. Xie, Y. Li, Q. Wang, et al., Carbon Energy 2 (2020) 540–560.
[9] Q. Liu, H. Zhang, J. Xie, X. Liu, X. Lu, Carbon Energy 2 (2020) 521–539.
[10] Q. Zhao, A. Song, S. Ding, et al., Adv. Mater. 32 (2020) 2002450.
[11] Y. Liu, X. Wu, Chin. Chem. Lett. 33 (2022) 1236–1244.
[12] Y. Li, Z. Wang, Y. Cai, et al., Energy Environ. Mater. 5 (2022) 1–29.
[13] W. Yang, W. Yang, Y. Huang, et al., Chin. Chem. Lett. 33 (2021) 4628–4634.
[14] P. Guo, G. Yang, C. Wang, J. Mater. Chem. A 9 (2021) 16868–16877.
[15] F. Cheng, H. Wang, Z. Zhu, et al., Energy Environ. Sci. 4 (2011) 3668–3675.
[16] X. Liang, H. Kim, H.G. Jung, Y.K. Sun, Adv. Funct. Mater. 31 (2021) 2008569.
[17] Y. Liu, C. Li, J. Xu, et al., Nano Energy 67 (2020) 104211.
[18] B. Xiao, Carbon Energy 2 (2020) 251–264.
[19] Q. Zhao, Z. Yan, C. Chen, J. Chen, Chem. Rev. 117 (2017) 10121–10211.
[20] R.W. Grimes, A.B. Anderson, A.H. Heuer, J. Am. Chem. Soc. 111 (1989) 1–7.
[21] J.B. Goodenough, A.L. Loeb, Phys. Rev. 98 (1955) 391–408.
[22] X. Yuan, T. Sun, S. Zheng, et al., J. Mater. Chem. A 8 (2020) 22686–22693.
[23] N. Zhang, F. Cheng, Y. Liu, et al., J. Am. Chem. Soc. 138 (2016) 12894–12901.
[24] K. Cai, S.H. Luo, J. Feng, et al., Chem. Record 22 (2022) e202100169.
[25] Z. Wang, H. Zhu, L. Ai, et al., Nanomaterials 11 (2021) 1122.
[26] S. Wang, Z. Ding, X. Wang, Chem. Commun. 51 (2015) 1517–1519.
[27] S. Curtarolo, G.L.W. Hart, M.B. Nardelli, et al., Nat. Mater. 12 (2013) 191–201.
[28] S. Curtarolo, W. Setyawan, G.L.W. Hart, et al., Computat. Mater. Sci. 58 (2012) 218–226.
[29] L. Kahle, A. Marcolongo, N. Marzari, Energy Environ. Sci. 13 (2020) 928–948.
[30] F. Ricci, A. Dunn, A. Jain, G.M. Rignanese, G. Hautier, J. Mater. Chem. A 8 (2020) 17579–17594.
[31] S. Kirklin, B. Meredig, C. Wolverton, Adv. Energy Mater. 3 (2013) 252–262.
[32] J. Cai, Z. Wang, S. Wu, Y. Han, J. Li, Energy Storage Mater. 42 (2021) 277–285.
[33] L. Ward, A. Dunn, A. Faghaninia, et al., Computat. Mater. Sci. 152 (2018) 60–69.
[34] A. Jain, S.P. Ong, G. Hautier, et al., APL Mater. 1 (2013) 011002.
[35] S.P. Ong, S. Cholia, A. Jain, et al., Comput. Mater. Sci. 97 (2015) 209–215.
[36] A. Jain, S.P. Ong, W. Chen, et al., Concurr. Comput. Pract. Exper. 27 (2015) 5037–5059.
[37] S.P. Ong, W.D. Richards, A. Jain, et al., Comput. Mater. Sci. 68 (2013) 314–319.
[38] T. Sun, H. Du, S. Zheng, Z. Tao, J. Power Sources 515 (2021) 230643.
[39] J.G. Wang, F. Kang, B. Wei, Prog. Mater Sci. 74 (2015) 51–124.
[40] J. Wang, J.G. Wang, H. Liu, Z. You, Z. Li, F. Kang, B. Wei, Adv. Funct. Mater. 31 (2021) 2007397.
[41] X. Wu, G. Liu, S. Yang, et al., Chin. Chem. Lett. 34 (2023) 107540.
[42] G. Fang, C. Zhu, M. Chen, et al., Adv. Funct. Mater. 29 (2019) 1808375.
[43] T. Wu, K. Zhu, C. Qin, K. Huang, J. Mater. Chem. A 7 (2019) 5612–5620.
[44] L. Zhou, A.M. Yao, Y. Wu, et al., Adv. Theory Simul. 4 (2021) 2100196.
[45] F. Tang, J. Gao, Q. Ruan, et al., Electrochim. Acta 353 (2020) 136570.
[46] J. Wang, J.G. Wang, X. Qin, et al., ACS Appl. Mater. Interfaces 12 (2020) 34949–34958.
[47] Y. Liao, H.C. Chen, C. Yang, et al., Energy Storage Mater. 44 (2022) 508–516.
[48] T. Shao, Y. Zhang, T. Cao, et al., Chem. Eng. J. 431 (2022) 133735.
[49] Y. Zhang, Y. Liu, Z. Liu, et al., J. Energy Chem. 64 (2022) 23–32.
[50] X. Liu, X. Shen, T. Chen, Q. Xu, J. Alloys. Compd. 904 (2022) 164002.
[51] S. Liu, L. Kang, J.M. Kim, et al., Adv. Energy Mater. 10 (2020) 2000477.
[52] M. Han, L. Qin, Z. Liu, et al., Mater. Today Energy 20 (2021) 100626.
[53] Y. Mo, S.P. Ong, G. Ceder, Chem. Mater. 24 (2012) 15–17.
[54] Q. Wenda, L. Yu, Y. Ao, et al., J. Mater. Chem. A 5 (2017) 14838–14846.
[55] S. Guo, S. Liang, B. Zhang, et al., ACS Nano 13 (2019) 13456–13464.
[56] J. Huang, X. Tang, K. Liu, et al., Mater. Today Energy 17 (2020) 100475.
[57] L. Ma, S. Chen, C. Long, X. Li, Y. Zhao, Z. Liu, Z. Huang, B. Dong, J.A. Zapien, C. Zhi, Adv. Energy Mater. 9 (2019) 1902446.
[58] B. Tang, J. Zhou, G. Fang, F. Liu, C. Zhu, C. Wang, A. Pan, S. Liang, J. Mater. Chem. A 7 (2019) 940–945.
[59] X. Yuan, T. Sun, S. Zheng, J. Bao, J. Liang, Z. Tao, J. Mater. Chem. A 8 (2020) 22686–22693.
[60] Z. Yang, X. Pan, Y. Shen, et al., Small 18 (2022) 2107743.
[61] W. Sun, F. Wang, S. Hou, et al., J. Am. Chem. Soc. 139 (2017) 9775–9778.
[62] X.Z. Zhai, J. Qu, J. Wang, et al., Energy Storage Mater. 42 (2021) 753–763.
[63] X.Z. Zhai, J. Qu, S.M. Hao, et al., Nano Micro Lett. 12 (2020) 56.
[64] Y. Tsuji, P.L.V.K. Dasari, S.F. Elatresh, R. Hoffmann, N.W. Ashcroft, J. Am. Chem. Soc. 138 (2016) 14108–14120.